

Deformed-Basis Antisymmetrized Molecular Dynamics and Its Application to ^{20}Ne

Masaaki Kimura

*RI-Beam Science Laboratory, RIKEN (The Institute of Physical
and Chemical Research), Wako, Saitama 351-0198, Japan.*

(Dated: November 15, 2018)

Abstract

A new theoretical framework is presented that uses a localized triaxially deformed Gaussian as the single-particle wave packet. The model space enables us to adequately describe both the deformed mean-field structure and the cluster structure within the same framework. The improvement over the original version of antisymmetrized molecular dynamics which uses the spherical Gaussian is verified by its application to the ^{20}Ne nucleus. The coexistence and interplay of the cluster structure and the deformed mean-field structure in the low-excited states of ^{20}Ne is studied. In particular, the intra-band $E2$ transition probabilities in $K^\pi=0_1^+$ and 2^- bands are reproduced without any effective charge.

PACS numbers: Valid PACS appear here

I. INTRODUCTION

In light nuclei up to the beginning of the *sd*-shell, the cluster structure is one of the most essential features of the nuclear structure together with a mean-field-like (shell-model-like) structure. On the heels of the cluster structure studies of the *p-sd* shell nuclei [1], many theoretical studies have been conducted to investigate the cluster aspects of the heavier *sd-pf* shell nuclei [2, 3]. Experimentally, some negative-parity levels which have large α -spectroscopic factors have been observed in ^{40}Ca and ^{44}Ti [4], and these states have been considered to be $K^\pi=0^-$ band members of the parity doublet bands with $K^\pi=0^+$ which have an α +core structure. It is of great interest and importance to survey the cluster aspect of these heavier isotopes, but the study seems to be in a rather intermediate stage. Another new field for cluster study is the unstable nucleus. Due to advances in experimental technique, many new aspects and phenomena such as neutron halo, neutron skin and the change of the magic number [5, 6] have been observed and studied, and now an increasing body of information on the unstable nuclei is available. It has been shown by many theoretical and experimental studies that the cluster-like correlation is also important and the exotic cluster structure which cannot be seen in stable isotopes appears in light neutron-rich isotopes. Therefore, new cluster aspects are expected in heavier stable and unstable nuclei.

One of the difficulties of cluster structure study in heavier nuclei is the existence and importance of the mean-field deformation of the nucleus, which should be properly treated together with clustering. It is quite conceivable that the mean-field deformation and clustering coexist, compete or are mixed. For the study of the nucleus in such situations, we have to treat the cluster structure and the deformed mean-field structure within the same framework. Another difficulty is the increasing importance of the spin-orbit force. The strong effect of the spin-orbit force will dissolve the cluster structure. Therefore the expectation value of the spin-orbit force can be regarded as a kind of measure that tells whether or not a cluster structure with doubly closed shell subunits develops. The importance of the spin-orbit force increases as we proceed to heavier nuclei.

To study the cluster aspects of heavier nuclei, we have introduced deformed-basis antisymmetrized molecular dynamics (deformed-basis AMD), which employs a localized triaxially deformed Gaussian as the single-particle wave packet [9]. In this work, we present the detailed framework of deformed-basis AMD and argue the advantages of this new framework.

In short, the present framework has two advantages. The first is its better description of the deformed mean-field achieved by making the single-particle wave packets deformable. The second is its improved incorporation of spin-orbit force effects. These advantages become clear in its application to the low-lying rotational bands of the ^{20}Ne nucleus.

The $K^\pi=0_1^\pm$ bands of ^{20}Ne are regarded as parity doublet bands with an $\alpha+^{16}\text{O}$ cluster structure. However, at the same time, the impurity of the $\alpha+^{16}\text{O}$ cluster structure in the ground band has been discussed by many authors, while the $K^\pi=0^-$ band is considered to have an almost pure $\alpha+^{16}\text{O}$ cluster structure. Indeed the intra-band $B(E2)$ values of the ground band have been underestimated by $\alpha+^{16}\text{O}$ cluster models. It is considered that this deficiency originates in the mixture of the deformed mean-field structure with an $\alpha+^{16}\text{O}$ cluster structure. The lowest negative-parity band is the $K^\pi=2^-$ band which has a $(0p)^{-1}(sd)^5$ structure. Unlike $K^\pi=0_1^\pm$ bands, this band should be understood in terms of the deformed mean-field. Thus, in the low-lying states of ^{20}Ne , the cluster structure and the deformed mean-field structure coexist and are mixed with each other. This intermingled situation has not been treated in a consistent manner within a full microscopic framework. It will be shown that the present framework is flexible enough to describe the coexistence and the mixture of the cluster structure and the deformed mean-field structure.

The contents of this article are as follows. In the next section, the framework of deformed-basis AMD is given and the calculational procedure adopted in this study is explained. The features and the advantages of this new framework are explained in the section III. The advantages in the practical calculation are shown by applying the method to the ^{20}Ne nucleus (section IV). In the course of this application, the characters of the low-lying rotational bands of ^{20}Ne , $K^\pi=0_1^+, 0_4^+, 0_1^-$ and 2^- bands are discussed, and the calculated results are examined. In the last section, we summarize this work.

II. FRAMEWORK OF DEFORMED-BASIS AMD

In this section, the framework of deformed-basis AMD is presented and the calculational procedure adopted in this study is explained. In the following, we call usual AMD, which uses a spherical Gaussian as the single-particle wave packet 'spherical-basis AMD' to keep the distinction clear. For a more detailed explanation of spherical-basis AMD framework, the reader is directed to references [13, 14].

A. Wave function and Hamiltonian

In deformed-basis AMD, the intrinsic wave function of the system with mass A is given by a Slater determinant of single-particle wave packets;

$$\Phi_{int} = \frac{1}{\sqrt{A!}} \mathcal{A}\{\varphi_1, \varphi_2, \dots, \varphi_A\}, \quad (1)$$

$$\varphi_i(\mathbf{r}) = \phi_i(\mathbf{r}) \chi_i \xi_i, \quad (2)$$

where φ_i is the i th single-particle wave packet consisting of spatial ϕ_i , spin χ_i and isospin ξ_i parts. Deformed-basis AMD employs the triaxially deformed Gaussian centered at \mathbf{Z}_i as the spatial part of the single-particle wave packet, while spherical-basis AMD limits the Gaussian to spherical shape:

$$\begin{aligned} \phi_i(\mathbf{r}) &\propto \exp \left\{ - \sum_{\sigma=x,y,z} \nu_{\sigma} (r_{\sigma} - Z_{i\sigma})^2 \right\}, \\ \chi_i &= \alpha_i \chi_{\uparrow} + \beta_i \chi_{\downarrow}, \quad |\alpha_i|^2 + |\beta_i|^2 = 1 \\ \xi_i &= \text{proton} \quad \text{or} \quad \text{neutron}. \end{aligned} \quad (3)$$

Here, the complex number parameter \mathbf{Z}_i which represents the center of the Gaussian in phase space takes an independent value for each nucleon. The width parameters ν_x, ν_y and ν_z are real number parameters and take independent values for each direction, but are common to all nucleons. Spin part χ_i is parametrized by α_i and β_i and isospin part ξ_i is fixed to up (proton) or down (neutron). $\mathbf{Z}_i, \nu_x, \nu_y, \nu_z$ and α_i, β_i are the variational parameters and are optimized by the method of frictional cooling explained in the next subsection. By using a deformed Gaussian basis, we can improve the description of deformed nuclei. The effects resulting from the deformed Gaussian basis are explained in the section III and are shown in its practical application to the ^{20}Ne (section IV). As the variational wave function, we employ the parity projected wave function in the same way as many other AMD studies [13, 14, 17],

$$\Phi^{\pm} = P^{\pm} \Phi_{int} = \frac{(1 \pm P_x)}{2} \Phi_{int}, \quad (4)$$

here P_x is the parity operator and Φ_{int} is the intrinsic wave function given in Eq(1).

The Hamiltonian used in this study is as follows;

$$\hat{H} = \hat{T} + \hat{V}_n + \hat{V}_c - \hat{T}_g, \quad (5)$$

where \hat{T} and \hat{T}_g are the kinetic energy and the energy of the center of mass motion, respectively. The expectation value of the \hat{T}_g is evaluated without any approximation, but the wave function contains the spurious component of the center-of-mass motion. Because the wave function of the center-of-mass also has a deformed Gaussian form, it becomes inseparable when the angular momentum is projected and/or the multiple Slater determinants are superposed. A prescription should be developed. In this study, we have approximated its influence by subtracting the expectation value of the center-of-mass kinetic energy. We have used the Gogny force D1S force as an effective nuclear force \hat{V}_n . Coulomb force \hat{V}_c is approximated by the sum of seven Gaussians.

B. Energy variation, angular momentum projection and generator coordinate method

We perform the variational calculation and optimize the variational parameters included in the trial wave function Eq(4) to find the state that minimizes the energy of the system E^\pm ;

$$E^\pm = \frac{\langle \Phi^\pm | \hat{\mathcal{H}} | \Phi^\pm \rangle}{\langle \Phi^\pm | \Phi^\pm \rangle}, \quad \hat{\mathcal{H}} = \hat{H} + \hat{V}_{cnst}. \quad (6)$$

We add the constraint potential \hat{V}_{cnst} to the Hamiltonian \hat{H} to obtain the minimum energy state under the optional constraint condition. In this study, we constrain matter quadrupole deformation by employing the potential $\hat{V}_{cnst} = v_{cnst}(\langle \beta^2 - \beta_0^2 \rangle^2)$ and we obtain the optimized wave function $\Phi^\pm(\beta_0) = P^\pm \Phi_{int}(\beta_0)$ as a function of the deformation parameter β_0 . The evaluation of the quadrupole deformation parameter β is explained in reference [17]. At the end of the variational calculation, the expectation value of V_{cnst} should be zero in principle, and in the practical calculations we confirm that it is less than 100 eV.

Energy variation of the AMD wave function is performed by the frictional cooling method, which is one of the imaginary time development methods. The reader is directed to references [13, 14] for a more detailed description. The time development equation for the complex number parameters \mathbf{Z}_i , α_i and β_i is as follows;

$$\frac{dX_i}{dt} = \frac{\mu}{\hbar} \frac{\partial}{\partial X_i^*} \frac{\langle \Phi^\pm | \hat{\mathcal{H}} | \Phi^\pm \rangle}{\langle \Phi^\pm | \Phi^\pm \rangle}, \quad (i = 1, 2, \dots, A) \quad (7)$$

and for the real number parameters ν_x , ν_y and ν_z ;

$$\frac{d\nu_\sigma}{dt} = \frac{\mu'}{\hbar} \frac{\partial}{\partial \nu_\sigma} \frac{\langle \Phi^\pm | \hat{\mathcal{H}} | \Phi^\pm \rangle}{\langle \Phi^\pm | \Phi^\pm \rangle}, \quad (\sigma = x, y, z) \quad (8)$$

Here X_i is \mathbf{Z}_i , α_i , or β_i . μ and μ' are arbitrary negative real numbers. It is easy to show that the energy of the system decreases as time develops, and after sufficient time steps we obtain the minimum energy state.

From the optimized wave function, we project out the eigenstate of the total angular momentum J ,

$$\Phi_{MK}^{J\pm}(\beta_0) = P_{MK}^J \Phi^\pm(\beta_0) = P_{MK}^{J\pm} \Phi_{int}(\beta_0). \quad (9)$$

Here P_{MK}^J is the total angular momentum projector. The integrals over the three Euler angles included in the P_{MK}^J are evaluated by numerical integration.

Furthermore, we superpose the wave functions $\Phi_{MK}^{J\pm}$ which have the same parity and angular momentum but have different values of deformation parameters β_0 and K . Thus the final wave function of the system becomes as follows:

$$\Phi_n^{J\pm} = c_n \Phi_{MK}^{J\pm}(\beta_0) + c'_n \Phi_{MK'}^{J\pm}(\beta'_0) + \dots, \quad (10)$$

where quantum numbers other than total angular momentum and parity are represented by n . The coefficients c_n , c'_n , ... are determined by the Hill-Wheeler equation,

$$\delta(\langle \Phi_n^{J\pm} | \hat{H} | \Phi_n^{J\pm} \rangle - \epsilon_n \langle \Phi_n^{J\pm} | \Phi_n^{J\pm} \rangle) = 0. \quad (11)$$

It is sometime useful to include the intrinsic wave function obtained from the variational calculation after the projection to the opposite parity. For instance, suppose that $\Phi_{int(+)}(\beta_0)$ and $\Phi_{int(-)}(\beta_0)$ are the intrinsic wave functions obtained by the variational calculation after the projection to positive- and negative-parity, respectively. We include $P_{MK}^{J+} \Phi_{int(-)}(\beta_0)$ in the GCM basis as well as $P_{MK}^{J+} \Phi_{int(+)}(\beta_0)$ to describe the positive-parity state Φ_n^{J+} ;

$$\begin{aligned} \Phi_n^{J+} = & c_n P_{MK}^{J+} \Phi_{int(+)}(\beta_0) + c'_n P_{MK'}^{J+} \Phi_{int(+)}(\beta'_0) + \dots \\ & + c''_n P_{MK''}^{J+} \Phi_{int(-)}(\beta''_0) + c'''_n P_{MK'''}^{J+} \Phi_{int(-)}(\beta'''_0) + \dots \end{aligned} \quad (12)$$

In the present study, we have employed all of the intrinsic wave functions on the obtained positive- and negative-parity energy curves as the GCM basis.

III. FEATURES AND ADVANTAGES OF THE PRESENT MODEL

The framework of AMD has some advantages over other theoretical methods. For instance, parity projection before the variation, angular momentum projection after (before) the variation and superposition of the Slater determinants (GCM) are easily executable in this framework. It is well known that parity projection is essentially important to describe the parity asymmetric shape of the nucleus and parity asymmetric cluster structure [14, 15]. Angular momentum projection and superposition of Slater determinants are indispensable to study the level scheme of the nucleus and the nuclear-structure-change in each state beyond the mean-field picture. In this section, besides these advantages which are common to spherical- and deformed-basis AMD, we explain the features and advantages of deformed-basis AMD in the study of the heavier nuclei. First, we discuss the description of the deformed mean-field structure and cluster structure in this model. Then we discuss the evaluation of the spin-orbit force.

A. Deformed mean-field structure and cluster structure

In deformed-basis AMD, deformed mean-field structure is described by deformed single-particle wave packets and the centroids of single-particle wave packet \mathbf{Z}_i gathered to the center of the nucleus, while the cluster structure is described by the localization of \mathbf{Z}_i s into several parts of the coordinate space.

Roughly speaking, in deformed-basis AMD, the change of nuclear shape as a function of nuclear deformation is classified into three patterns as sketched in FIG. 1. In this figure, for the sake of simplicity, we consider only the elliptical deformation of the mean-field and the cluster structure consisting of two spherical subunits. The first pattern shows deformation of the mean-field (FIG. 1, (i)). When the nuclear deformation becomes larger, only the deformation of the mean-field becomes larger. In this case, all \mathbf{Z}_i in Eq(3) are gathered in the small region around the center of nucleus and the single-particle wave packets are deformed. In this limit, the nuclear deformation is described by the deformation of the single-particle wave packets and the strong effect of the Pauli principle (single particle motion in the deformed mean-field). In other words, the intrinsic wave function Eq. (1) contains a large amount of the deformed shell model configurations. This structure is not described

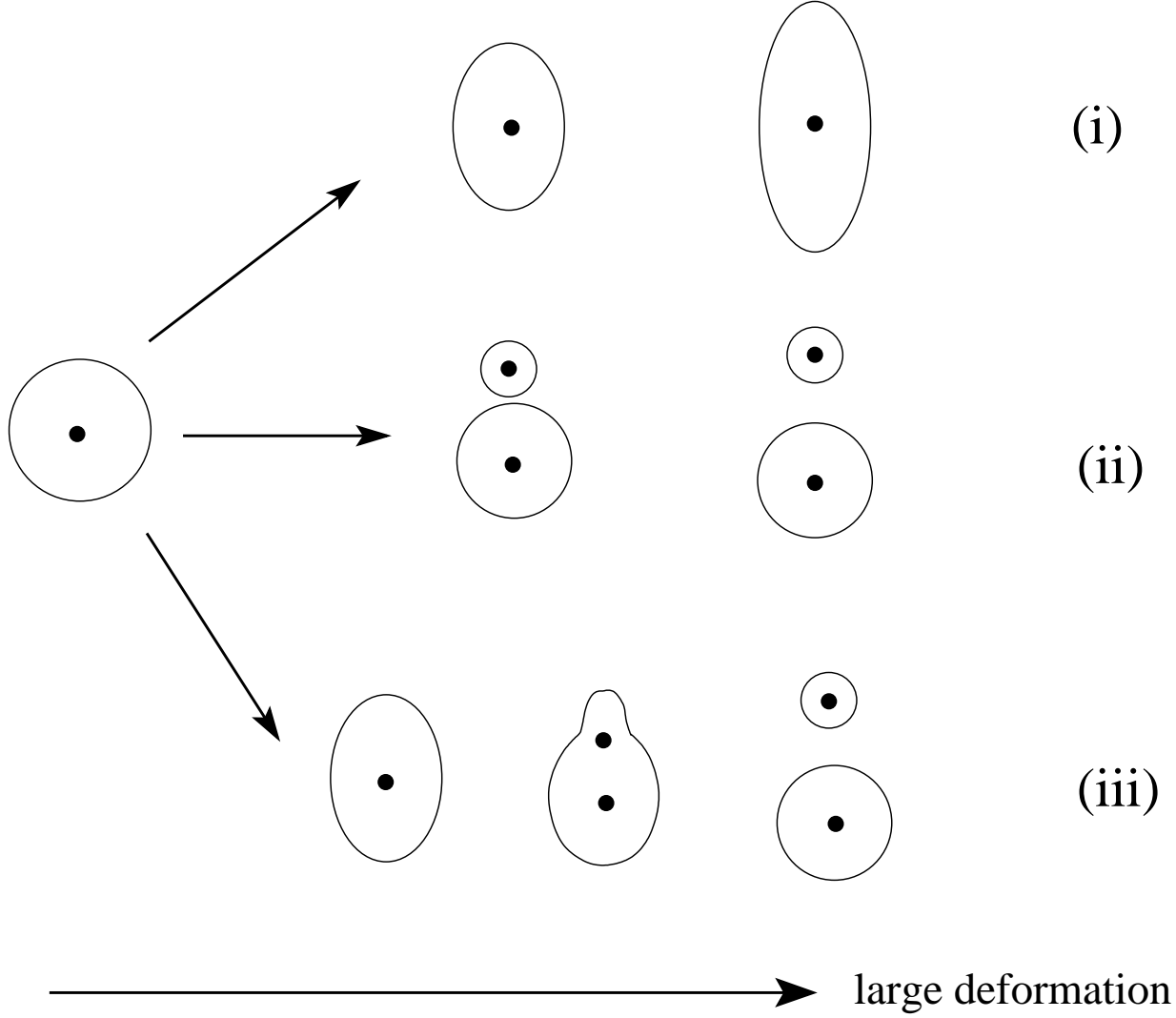


FIG. 1: Schematic figure showing three different patterns of the nuclear deformation in deformed-basis AMD. Points in the figure indicate the centroids of the single-particle wave packets ($\text{Re}(\mathbf{Z}_i)$) of a deformed-basis AMD wave function.

well by spherical-basis AMD and this is the reason that spherical-basis AMD sometimes provides an inadequate description of deformed heavier nuclei [16]. The second pattern (FIG. 1, (ii)) shows the deformation caused by clustering. In this pattern, the nucleus splits into two clusters. This structure is described by the localization of \mathbf{Z}_i into two parts and the spherical shape of the single-particle wave packets. As the nuclear deformation becomes larger, the distance between two clusters becomes larger, but the single-particle wave packets remain spherical. The third pattern (FIG. 1, (iii)) has a mixed character of (i) and (ii). At small deformations, the nucleus has a mean-field character, but as the deformation becomes

larger, a cluster-like structure grows and the nucleus has an intermediate character. At large deformations, it changes to an almost pure cluster structure. In the application to ^{20}Ne , it will be shown that $J^\pi=2^-(K^\pi=2^-)$, $1^-(K^\pi=0^-)$ and $0^+(K^\pi=0^+)$ curves correspond to patterns (i),(ii) and (iii), respectively.

B. Evaluation of the spin-orbit force

In medium-heavy nuclei, the importance of the spin-orbit force increases. In short, the spin-orbit force acts to dissolve the cluster structure. Since spherical-basis AMD does not assume any cluster structure, it can describe the dissociation of the cluster structure due to the spin-orbit force. However, it was pointed out that in heavier isotopes, the spherical-basis AMD wave function provides a much smaller expectation value of the spin-orbit force compared to HF theory when the same interaction Skyrme III force is adopted [16]. We consider that this is because single-particle wave packets are limited to the spherical Gaussian form in spherical-basis AMD. Since the spin-orbit force contains the derivative operator, it is sensitive to the slope and the deformation of the single-particle wave packet. When the system favors the mean-field deformation, doubly closed-shell clusters such as α and ^{16}O clusters are difficult to form. This often means that deformed-basis AMD gives us larger expectation values of the spin-orbit force than spherical-basis AMD does, because the latter tends to give us a larger amount of the clustering component in the system wave function than the former. For instance, deformed-basis AMD gives twice as large an expectation value of the spin-orbit force (-19.0 MeV) as spherical-basis AMD gives (-11.6 MeV) in the ^{24}Mg nucleus. In contrast, when a nucleus favors a cluster structure consisting of doubly-closed-shell subunits like $K^\pi=0^-$ band of ^{20}Ne , spin-orbit force does not act at all and the shape of the single-particle wave packet is not distorted by it. Therefore, the expectation value of the spin-orbit force can be regarded as a type of measure that identifies the formation and dissociation of the cluster structure. In the next section, it will be shown that the different characters of the rotational bands of ^{20}Ne are directly reflected in the expectation value of the spin-orbit force.

IV. APPLICATION TO ^{20}Ne AND DISCUSSION

We have applied the present framework to the ^{20}Ne nucleus to study the coexistence and mixing of the cluster structure and the deformed mean-field structure. First, we investigate the structure change of the wave functions as a function of matter quadrupole deformation. Then we study the detailed properties of each band.

A. Overview of the energy curves

After the variational calculation and the angular momentum projection to the $J^\pi=0^+$ ($K^\pi=0^+$), 1^- ($K^\pi=0^-$) and 2^- ($K^\pi=2^-$), we obtain three energy curves as functions of the deformation parameter β (FIG. 2). In the positive-parity state, we obtain the $J^\pi=0^+$ curve (solid line with circles in FIG. 2), and when we perform the GCM calculation, $J^\pi=0_1^+$ and $J^\pi=0_4^+$ states are mainly obtained from this curve. Similarly, $J^\pi=2_1^+$ and $J^\pi=2_4^+$ states are obtained by superposing the wave functions on the $J^\pi=2^+$ ($K^\pi=0^+$) curve and so on for other higher spin states. In the negative-parity state, we obtain the $J^\pi=1^-$ curve (dashed line with triangle) and 2^- curve (dotted line with boxes) which mainly contribute to the $J^\pi=1^-$ ($K^\pi=0_1^-$) and $J^\pi=2^-$ ($K^\pi=2^-$) states, respectively. Detailed results of the GCM calculation are given in the next subsection, and in this subsection, we concentrate on the $J^\pi=0^+$, 0^- and 2^- curves to discuss the different nature of the wave functions. The results obtained by spherical-basis AMD are also plotted for comparison (lines without marks). Three patterns of the nuclear shape change mentioned in the previous section can be seen on these three energy curves obtained by deformed-basis AMD. When we compare the $J^\pi=1^-$ ($K^\pi=0^-$) curve of deformed-basis AMD with that of spherical-basis AMD, they are almost identical, while there are differences in the position of the minimum energy point and in the minimum energy in the $J^\pi=2^-$ ($K^\pi=2^-$) curves. In deformed-basis AMD, the $J^\pi=2^-$ curve has a minimum energy point around $\beta=0.45$, but in spherical-basis AMD, it has an unclear minimum energy point around $\beta=0.25$ and its energy is underestimated by about 5 MeV compared with deformed-basis AMD. These similarity and difference are due to the different nature of the $J^\pi=1^-$ and 2^- curves. The $J^\pi=1^-$ curve has an almost pure cluster structure, while the $J^\pi=2^-$ curve has a deformed mean-field structure. Since the cluster structure is well described by both spherical- and deformed-basis AMD, there is no

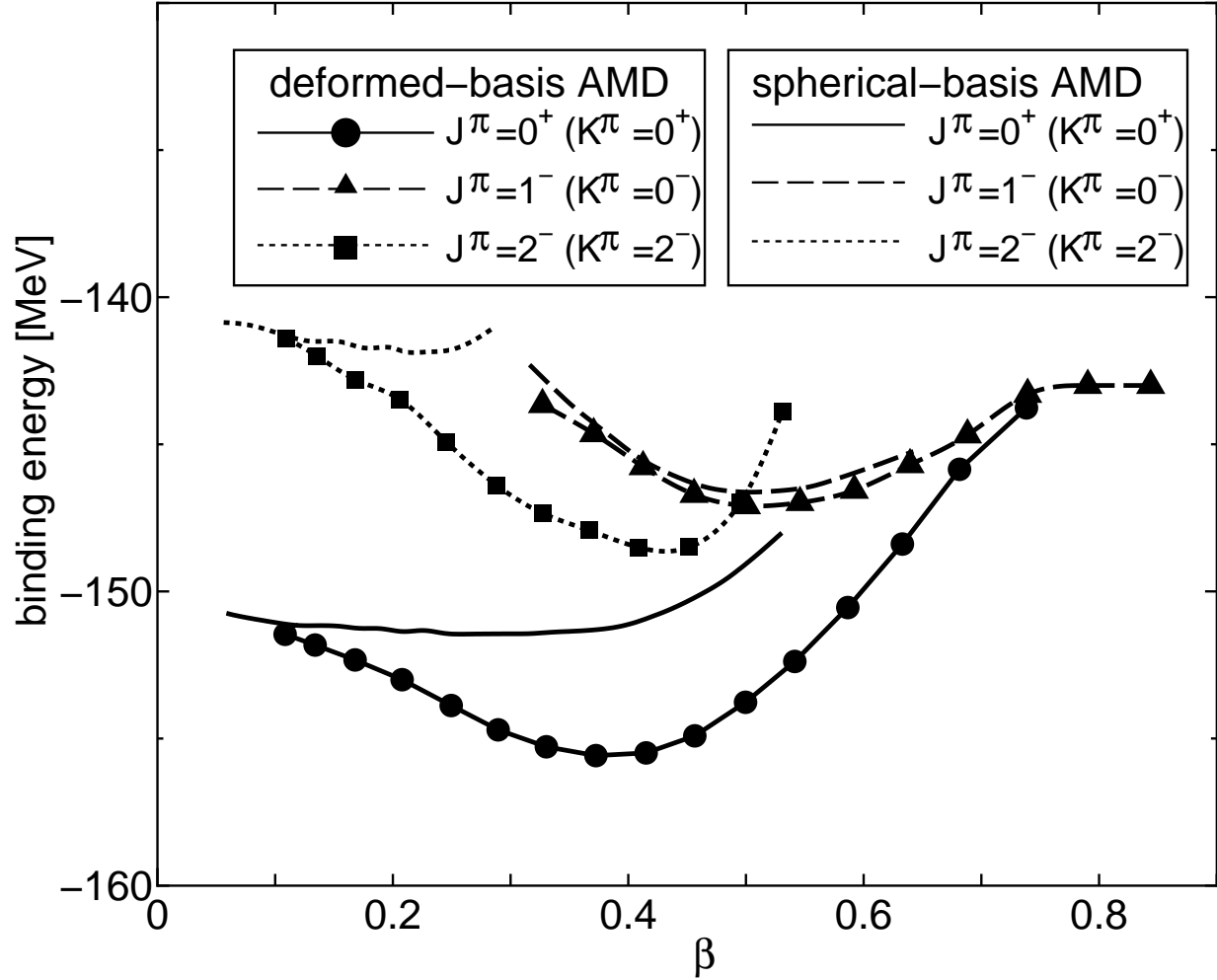


FIG. 2: β -energy curves of ^{20}Ne (energy curves as a function of the deformation parameter β). Lines with symbols (Lines) are the result of deformed-basis AMD (spherical-basis AMD). $K^\pi=0^+$ and $K^\pi=2^-$ states are more deeply bound in deformed-basis AMD than in spherical-basis AMD (See text).

difference in their description of the $J^\pi=1^-$ curve. However, because deformed-basis AMD can describe the deformed mean-field structure better than spherical-basis AMD, there is a difference in the description of the $J^\pi=2^-$ curve. The different nature of these two states becomes clear in the deformation of the single-particle wave packets and in the distributions of the centroids of the single-particle wave packets. In the $J^\pi=1^-$ curve (dashed line in FIG. 3), single-particle wave packets are always almost spherical but the centroids of the twenty single-particle wave packets (black points in FIG. 4 (d) and (e)) are widely separated into two subunits, α (four points degenerate on the upper side) and ^{16}O (sixteen points are almost

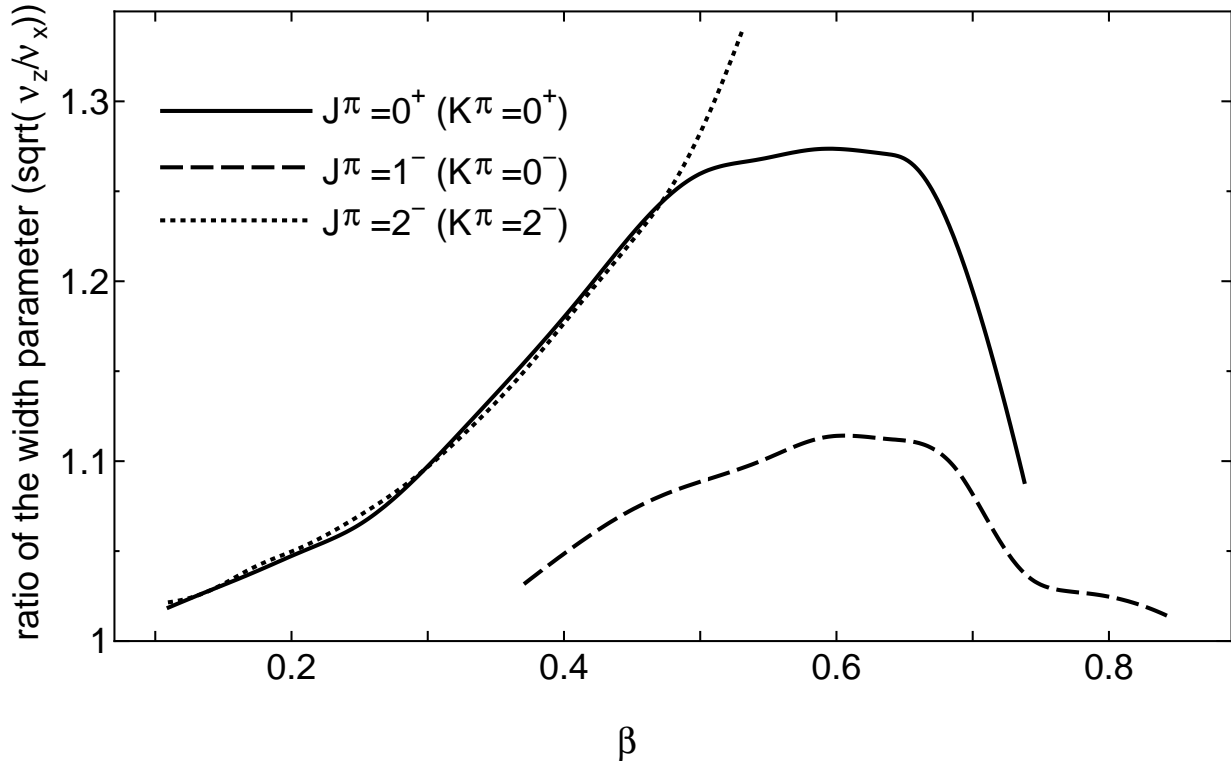


FIG. 3: The ratio of the width parameter of the single-particle wave packet ($\sqrt{\nu_z/\nu_x}$) as a function of the deformation parameter β . In the present calculation, the single-particle wave packets are always almost axially symmetric and z axis is taken to be the symmetry axis.

degenerate in the middle). As the nuclear deformation becomes larger, only the distance between two subunits becomes larger. Therefore, this nuclear shape change corresponds to the second pattern in FIG. 1. In contrast, in the $J^\pi=2^-$ curve, the single-particle wave packets are significantly deformed, as a function of the nuclear deformation (dotted line in FIG. 3). All of the centroids of the twenty single-particle wave packets are gathered around the center of the nucleus (FIG. 4 (f) and (g)), even though the nuclear deformation becomes larger. We note that though the nuclear deformation is larger in wave function (g) than in wave function (d), the centers of the single-particle wave packets are crowded into the center of the nucleus in wave function (g). Therefore, this state corresponds to the first pattern in FIG. 1 and shows a deformed mean-field nature. These different characters of the $J^\pi=1^-$ and 2^- curves are directly reflected in the expectation value of the spin-orbit force (FIG. 5). The spin-orbit force does not act at all in this state (dashed line with triangle in FIG. 5). However, it acts strongly in the $J^\pi=2^-$ wave function (dotted line with boxes) which has an

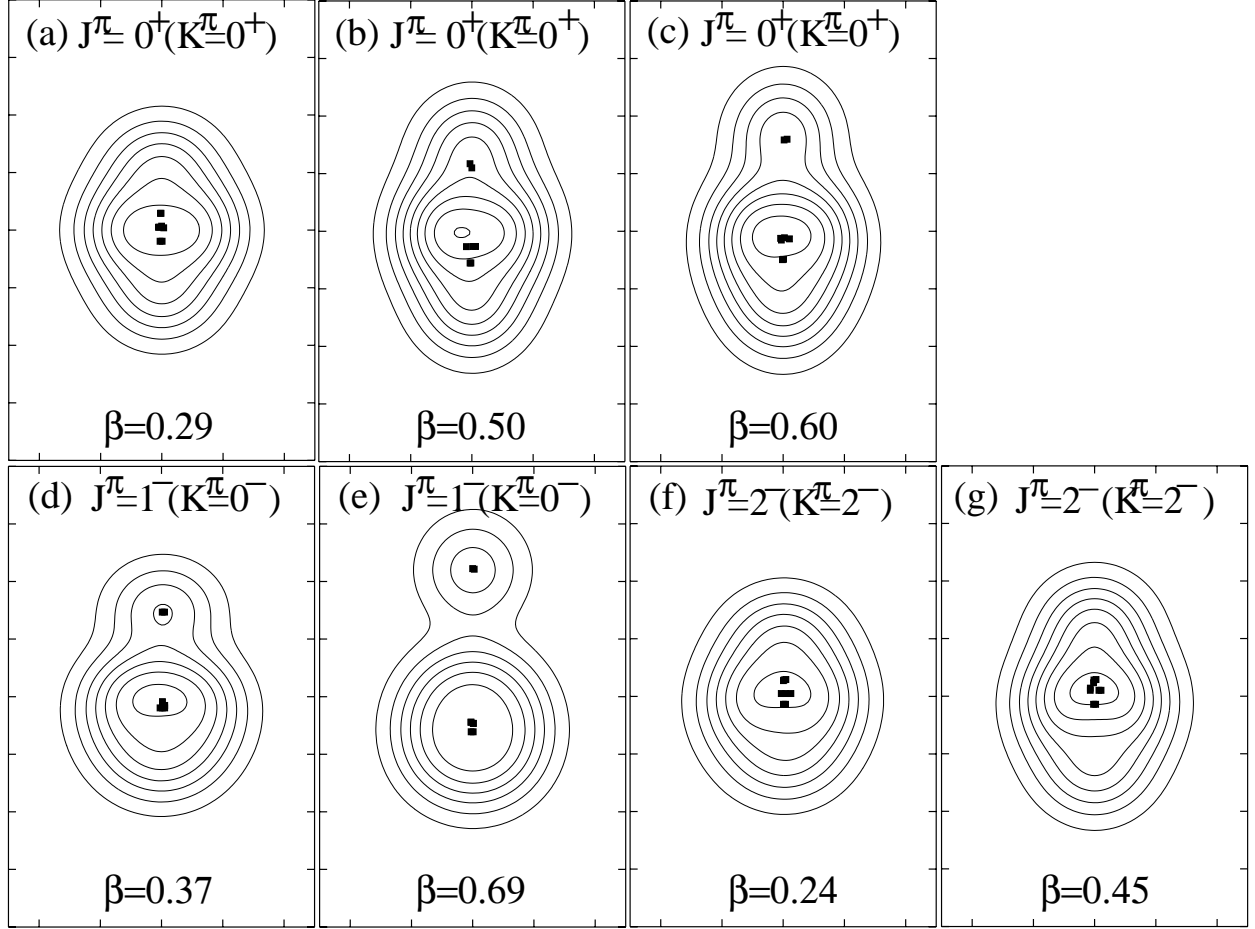


FIG. 4: The density distributions of the intrinsic wave functions on the energy curve obtained by the deformed-basis AMD. Twenty centroids of single-particle wave packets ($\text{Re } \mathbf{Z}_i$, $i=1 \sim 20$) are denoted by the black points in each panel. (a), (b) and (c) are for the $J^{\pi}=0^+$ ($K^{\pi}=0^+$) state, (d) and (e) are for the $J^{\pi}=1^-$ ($K^{\pi}=0^-$) states, and (f) and (g) are for the $J=2^-$ ($K^{\pi}=2^-$) states.

$(0p)^{-1}(sd)^5$ structure. The $(0p)^{-1}(sd)^5$ structure of the calculated $J^{\pi}=2^-$ state is confirmed by investigating the structure of the single-particle orbit. The technique for studying a single-particle orbit structure within the AMD framework was developed by Dóte, et al [17].

The energy curve for the $J^{\pi}=0^+$ state is more deeply bound about 5 MeV at the minimum energy point in deformed-basis AMD than in spherical-basis AMD. The intermediate character of the $J^{\pi}=0^+$ curve is confirmed in the deformation and distribution of single-particle wave packets. In this curve, the deformation of single-particle wave packets (solid line in FIG. 3) becomes larger as the nuclear deformation becomes larger in the small- and medium-deformation region ($\beta < 0.5$). In this stage, the centroids of the single-particle

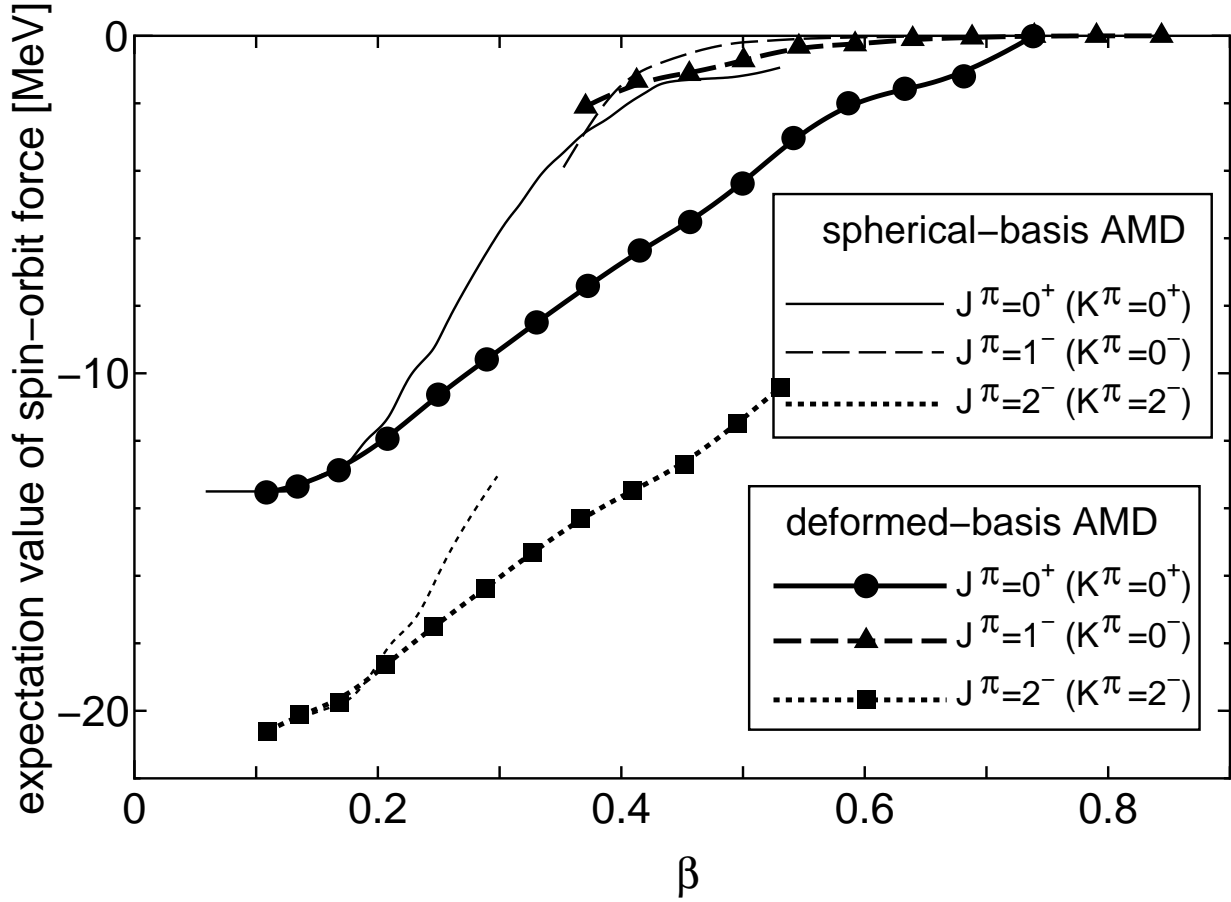


FIG. 5: The expectation value of the spin-orbit force for each parity projected wave function $\Phi^{J\pm}(\beta)$ are plotted as functions of the deformation parameter β . Lines with symbols (Lines) are the result of the deformed-basis AMD (spherical-basis AMD).

wave packets are gathered around the center of the nucleus (FIG. 4(a)) and the nucleus has a deformed mean-field character. But the deformation of the single-particle wave packets is saturated around $\beta \sim 0.5$. At this stage, the centroids of the single-particle wave packets are separated into α and ^{16}O parts (FIG. 4(b)), though the distance between them is rather small (about 1fm). Therefore, the nucleus has a good amount of $\alpha+^{16}\text{O}$ cluster component, although the cluster structure is distorted by the deformed mean-field structure. After this stage, the distance between the two subunits becomes larger, as the nuclear deformation becomes larger, while the deformation of the single-particle wave packets does not change. Then around $\beta \sim 0.65$, the distortion eases and the single-particle wave packets rapidly become spherical. Thus, the $J^\pi=0^+$ curve corresponds to the third pattern in FIG. 1. This change of nuclear shape and structure as a function of the deformation parameter β takes

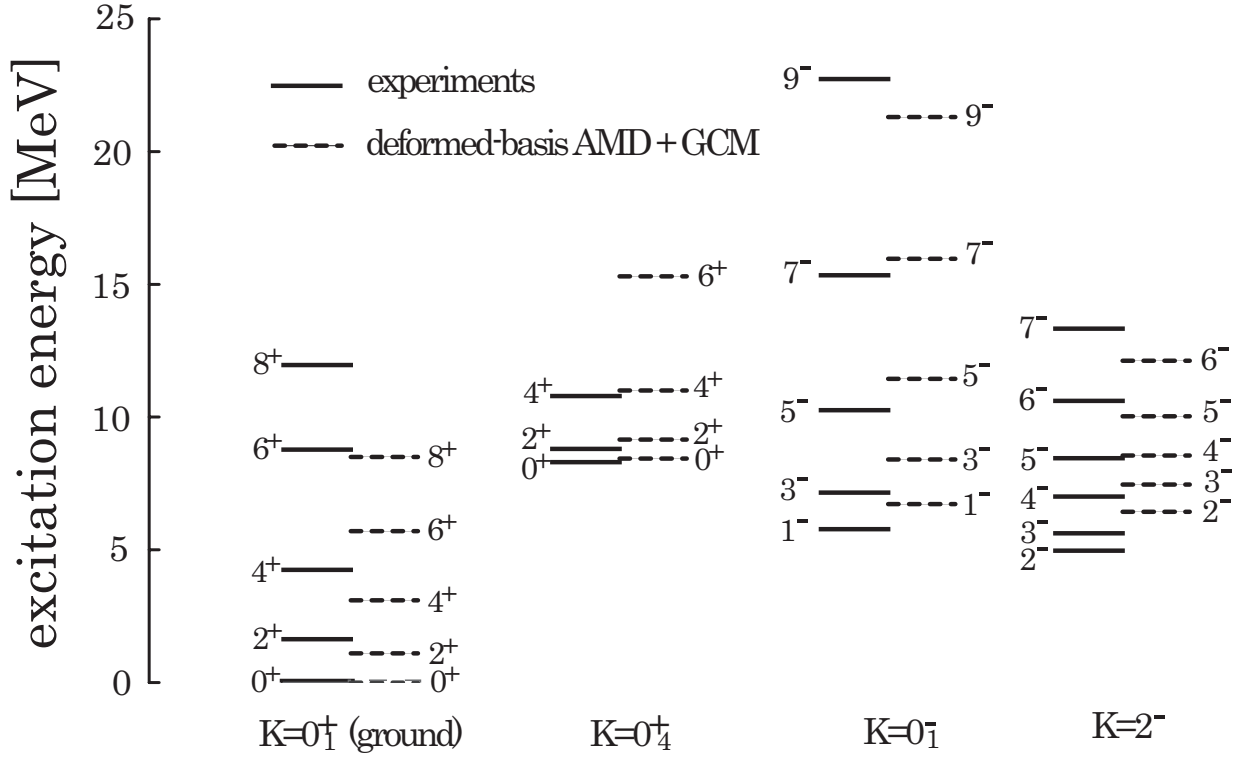


FIG. 6: The excitation energies of the low-lying states of ^{20}Ne . The observed values (the results of the deformed-basis AMD+GCM calculation) are given by the solid lines (dashed lines). The spin-parity of each state is also shown.

place gradually in the case of deformed-basis AMD. Therefore, the expectation value of the spin-orbit force decreases uniformly in deformed-basis AMD, while in spherical-basis AMD it becomes zero rather rapidly.

B. Low-lying level structure in ^{20}Ne

After the angular momentum projection, we perform the GCM calculation by superposing all of the wave functions on the obtained energy curves, and calculate the level scheme of ^{20}Ne (FIG. 6). We have obtained two $K^\pi=0^+$ bands in positive-parity and $K^\pi=2^-$ and $K^\pi=0_1^-$ bands in negative-parity. In this subsection, we discuss the detailed character of these bands and show the related quantities in due order.

TABLE I: Observed and calculated α -RW (θ_α^2), multiplied by 100 at the channel radius $a = 6\text{fm}$, for $K^\pi=0_1^+$, 0_4^+ and 0_1^- band members. For comparison, the results of the $(sd)^4$ shell model (SM) [18], $\alpha+^{16}\text{O}$ RGM (RGM) [19] and $(\alpha+^{16}\text{O})+(^{8}\text{Be}+^{12}\text{C})$ coupled channel OCM (OCM) [20] are shown.

K^π	J^π	$\theta_{obs}(a)^2 \times 100$	SM	RGM	OCM	AMD
0_1^+	6_1^+	1.0 ± 0.2	0.20	1.4	0.50	0.53
	8_1^+	0.094 ± 0.027	0.020	0.24	0.10	0.08
0_1^-	1^-	>16		34	22.2	31.0
	3_2^-	26		34	15.0	29.1
	5_2^-	30		36	11.5	28.8
	7_2^-	22 ± 5		33	12.5	11.5
	9^-	17		20	3.6	8.9
0_4^+	0_4^+	>50			139	69.0
	2_4^+	>59			80	68.0
	4_4^+	23			115	35.5

TABLE II: The squared amplitude of the $\alpha+^{16}\text{O}$ component W^J (see appendix) and the expectation value of the spin-orbit force $\langle \hat{V}_{ls} \rangle$ (in MeV) of the GCM wave function for each state.

K^π	J^π	W^J	$\langle \hat{V}_{ls} \rangle$	K^π	J^π	W^J	$\langle \hat{V}_{ls} \rangle$
0_1^+	0_1^+	0.70	-5.2	0_1^-	1_1^-	0.95	-0.8
	2_1^+	0.68	-5.3		3_2^-	0.93	-0.8
	4_1^+	0.54	-5.9		5_2^-	0.88	-0.7
	6_1^+	0.34	-8.4		7_2^-	0.71	-0.9
	8_1^+	0.28	-10.9		9_2^-	0.70	-1.3
0_4^+	0_4^+	0.82 (0.71)	-3.2	2^-	2_1^-		-12.9
	2_4^+	0.81 (0.71)	-3.0		3_1^-		-13.0
	4_4^+	0.79 (0.57)	-4.9		4_1^-		-14.1
	6_4^+	0.67 (0.37)	-6.8		5_1^-		-14.4
	8_4^+	0.55 (0.38)	-7.4		6_1^-		-16.5

1. $K^\pi = 0_1^-$ band

Experimentally, the $K^\pi=0_1^-$ band is built upon the 1^- state at 5.78 MeV, that is 1.05 MeV above the $\alpha+^{16}\text{O}$ threshold. In the present calculation, the excitation energy of the 1^- state is 6.72 MeV and the excitation energies of the higher spin states show good agreement with the observed values.

The $K^\pi=0_1^-$ band is regarded as having an almost pure $\alpha+^{16}\text{O}$ cluster structure, since the band members have large α decay widths comparable with the Wigner limit. Indeed, in the present calculation, the obtained α decay widths are large enough to be comparable with the observed values (Table. I) and the wave functions of the member states have quite large amounts of the $\alpha+^{16}\text{O}$ component (Table. II). The definitions and the method to evaluate these quantities are given in the Appendix. The almost pure cluster structure of this band is due to a dominant contribution from the wave functions on the $K^\pi=0^-$ ($J^\pi=1^-, 3^-, \dots$) energy curves. As is discussed in the previous subsection, the wave functions on the $J^\pi=0^-$ energy curve have an almost pure $\alpha+^{16}\text{O}$ cluster structure (and this character is common to other J^π curves with $K^\pi=0^-$). As a consequence, the member states of this band have an almost pure $\alpha+^{16}\text{O}$ cluster structure and small expectation values of the spin-orbit force (Table. II). Though we did not make any assumptions about the cluster structure in our calculation, the band members have almost pure cluster structures. This fact means that the cluster structure can exist as an independent degree of freedom of nuclear excitation, even though the effects of the spin-orbit force and the deformation of the mean-field are taken into account in the model space.

The relative motions between α and ^{16}O clusters were also investigated following the traditional cluster model studies. The α reduced width amplitudes $\mathcal{Y}_L(a)$ (α -RWA) are shown in Fig. 7 (dotted lines). The definitions and the calculational procedure for the α -RWA are also presented in the appendix. As in other cluster studies, it is clear that $K^\pi=0_1^-$ band members belong to the $N = 2n + L = 9$ band members of the $\alpha+^{16}\text{O}$ cluster structure. Here, N denotes the principal quantum number of relative motion and n denotes the radial quantum number (number of nodes). We also see that relative motion is suppressed inside of the nucleus and enhanced outside, which induces large intra-band $E2$ transition probabilities (Table. III).

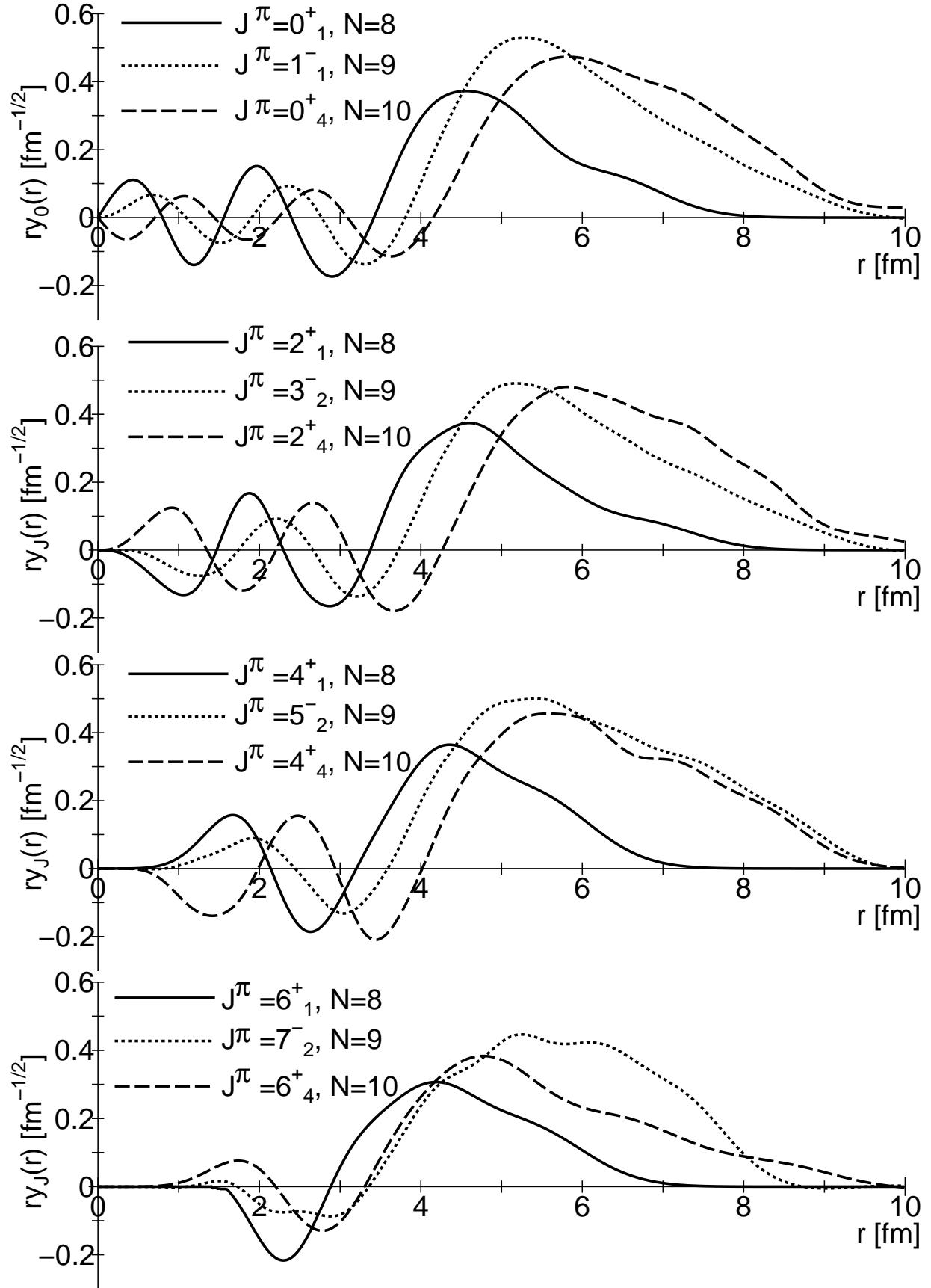


FIG. 7: The α -RWA for the member states of the $K^\pi=0^+_1$ (solid lines), 0^+_4 (dashed lines) and 0^-_1 (dotted lines) bands. See text and the appendix .

TABLE III: Observed (EXP) and calculated (AMD) intra-band $E2$ transition probabilities $B(E2; J_i^\pi \rightarrow J_f^\pi)$ [$e^2 \text{fm}^4$] within the $K^\pi=0_1^-$ band. For comparison, $\alpha+^{16}\text{O}$ RGM (RGM) [19] and multicluster GCM (5α) [22] are also shown. The effective charges which are used in each calculation are given in the bottom line.

$J_i^\pi \rightarrow J_f^\pi$	EXP	RGM	5α GCM	AMD
$3^- \rightarrow 1^-$	164 ± 26	121.4	155	151.2
$5^- \rightarrow 3^-$		133.399	206	182.4
$7^- \rightarrow 5^-$		122.74		141.6
$9^- \rightarrow 7^-$		67.83		87.9
$\delta e/e$		0	0	0

2. Ground band ($K^\pi = 0_1^+$ band)

The obtained binding energy of the ground state is -159.8 MeV, which underestimates the observed value by about 0.8 MeV. The rotational character of the 0_1^+ , 2_1^+ and 4_1^+ states and the deviation from the rotational spectra of the 6_1^+ and 8_1^+ states are reproduced, though the obtained excitation energies are smaller than the observed values.

The ground band must be the parity doublet partner of the $K^\pi=0_1^-$ band, since the ground band is the only $K^\pi=0^+$ band below the $K^\pi=0_1^-$ band. However, at the same time, the existence of the deformed mean-field component in the ground band has been discussed. For example, if the pure $\alpha+^{16}\text{O}$ cluster structure of this band is assumed, the intra-band $E2$ transition probabilities are underestimated. Shell model calculation has shown the existence of broken symmetry components in the wave function that activates the spin-orbit force.

The GCM wave functions describing the member states of this band have a mixed character embodying both the cluster structure and the deformed mean-field structure. They have a dominant contribution from the wave functions on the $K^\pi=0^+$ ($J^\pi=0^+, 2^+, \dots$) curves. The GCM-amplitude of the 0_1^+ state is shown in FIG. 8 (solid line). The GCM-amplitude that serves as a kind of measurement of the contribution to the GCM wave function from each intrinsic wave function is defined as

$$|c_n^{J\pm}(\beta_0)|^2 \equiv |\langle \Phi_n^{J\pm} | \Phi_{MK}^{J\pm}(\beta_0) \rangle|^2, \quad (13)$$

where $\Phi_n^{J\pm}$ is the GCM wave function (Eq.10) and $\Phi_{MK}^{J\pm}(\beta_0)$ is the parity and angular mo-

TABLE IV: Observed (EXP) and calculated (AMD) intra-band $E2$ transition probabilities $B(E2; J_i^\pi \rightarrow J_f^\pi)$ [$e^2 \text{fm}^4$] within the $K^\pi=0_1^+$ band. For comparison, the results of the $(sd)^4$ shell model (SM) [12], $\alpha+^{16}\text{O}$ RGM (RGM) [19], $(\alpha+^{16}\text{O})+(^8\text{Be}+^{12}\text{C})$ coupled channel OCM (OCM) [20] and multicluster GCM (5 α GCM) are also shown. The effective charges which were used in each calculation are given in the bottom line.

$J_i^\pi \rightarrow J_f^\pi$	EXP	SM	RGM	OCM	5 α GCM	AMD
$2_1^+ \rightarrow 0_1^+$	65 ± 3	57.0	36.2	57.0	50.0	70.3
$4_1^+ \rightarrow 2_1^+$	71 ± 6	69.9	45.22	70.9	64.4	83.7
$6_1^+ \rightarrow 4_1^+$	64 ± 10	57.9	36.5	57.1	55.3	52.7
$8_1^+ \rightarrow 6_1^+$	29 ± 4	35.5	19.7	34.8		21.0
$\delta e/e$		0.54	0	0.155	0	0

mentum projected wave function (Eq.9). The GCM-amplitude reaches a maximum around $\beta \sim 0.50$ in the low spin state and is larger than 50% from $\beta \sim 0.20$ to $\beta \sim 0.70$. As is shown in the previous subsection, the intrinsic wave function on the $J^\pi=0^+$ curve starts to change its structure from a deformed mean-field-like structure to a cluster structure around $\beta=0.5$. Therefore, unlike the $K^\pi=0_1^-$ band, the $K^\pi=0_1^+$ band is a mixture of the cluster structure and the deformed mean-field structure. Indeed, the wave functions of the ground band have smaller overlap with the $\alpha+^{16}\text{O}$ model space than the $K^\pi=0_1^-$ band (Table.II). This transient nature of the ground band is reflected in the expectation value of the spin-orbit force, which amounts to about -5.0 MeV in the ground state and increases as the angular momentum increases. The increase of the spin-orbit force contribution is a consequence of the structure change along the yrast line or the anti-stretching phenomenon, which is discussed later.

The transient nature of the ground band affects the intra-band $E2$ transition probabilities (Table.IV). They are successfully described quantitatively by the cluster models (RGM [19] and coupled channel OCM [20]), but they need to introduce a small effective charge. When the model space is expanded to include the $\alpha+^{16}\text{O}(0^+, 3^-, 1^-)$ channels (multicluster GCM)[22], the deformation of the mean-field is described to some extent and the result is improved. In the present calculation, the $E2$ transition probabilities of the ground band are described well without any effective charges. Therefore, we can conclude that the general

trend of the intra-band $E2$ transition probabilities are well described qualitatively by the $\alpha+^{16}\text{O}$ cluster component in the wave functions and the existence of the deformed mean-field component (or the cluster dissociated component) slightly enlarges the intra-band $E2$ transition probabilities.

Another important feature of the $\alpha+^{16}\text{O}$ cluster structure is the anti-stretching phenomenon, which is studied by many cluster models [1]. As the angular momentum increases, the $\alpha+^{16}\text{O}$ cluster structure moderates and the average distance between α and ^{16}O becomes smaller. Indeed, in the present result, the position of the maximum peak of the α -RWA moves slightly toward the inside of the nucleus as the angular momentum increases, though the tendency is rather mild. However, we wish to emphasize the difference of the anti-stretching phenomenon described by the $\alpha+^{16}\text{O}$ cluster models and the present model. In the $\alpha+^{16}\text{O}$ cluster models, the anti-stretching phenomenon is described by the decreasing distance between α and ^{16}O . However, in the present model, as the angular momentum increases, the $\alpha+^{16}\text{O}$ component diminishes and the spin-orbit force acts strongly. In particular, the 8_1^+ state is oblately deformed and four valence nucleons are aligned, which leads to a large contribution of the spin-orbit force which amounts to about -10 MeV, though a small amount of the $\alpha+^{16}\text{O}$ component survives outside of the nucleus. We also note that this remaining small amount of $\alpha+^{16}\text{O}$ component outside of the nucleus leads to the relatively large α decay widths of the $J^\pi=6_1^+$ and 8_1^+ states (Table. I).

3. $K^\pi=0_4^+$ band

The $K^\pi=0_4^+$ band has a prominent $\alpha+^{16}\text{O}$ cluster structure in which the relative motion between clusters is $2\hbar\omega$ excited ($N = 2n + L = 10$), while α and ^{16}O clusters are not excited. In the present calculation, the obtained second positive-parity band members have large amounts of $\alpha+^{16}\text{O}$ component and large α decay widths. Also, the relative motion between α and ^{16}O has the principal quantum number $N = 10$. Therefore, we identify this band as the $K^\pi=0_4^+$ band. The $K^\pi=0_2^+$ and 0_3^+ bands which do not have the $\alpha+^{16}\text{O}$ structure are not obtained in the present calculation, but we consider that we will obtain these two bands when we make the variational calculation and the GCM calculation in the model space which is orthogonal to the $K^\pi=0^+$ ($J^\pi=0^+, 2^+, \dots$) curves obtained in the present calculation. The calculated and observed excitation energy of the 0_4^+ state are 8.44

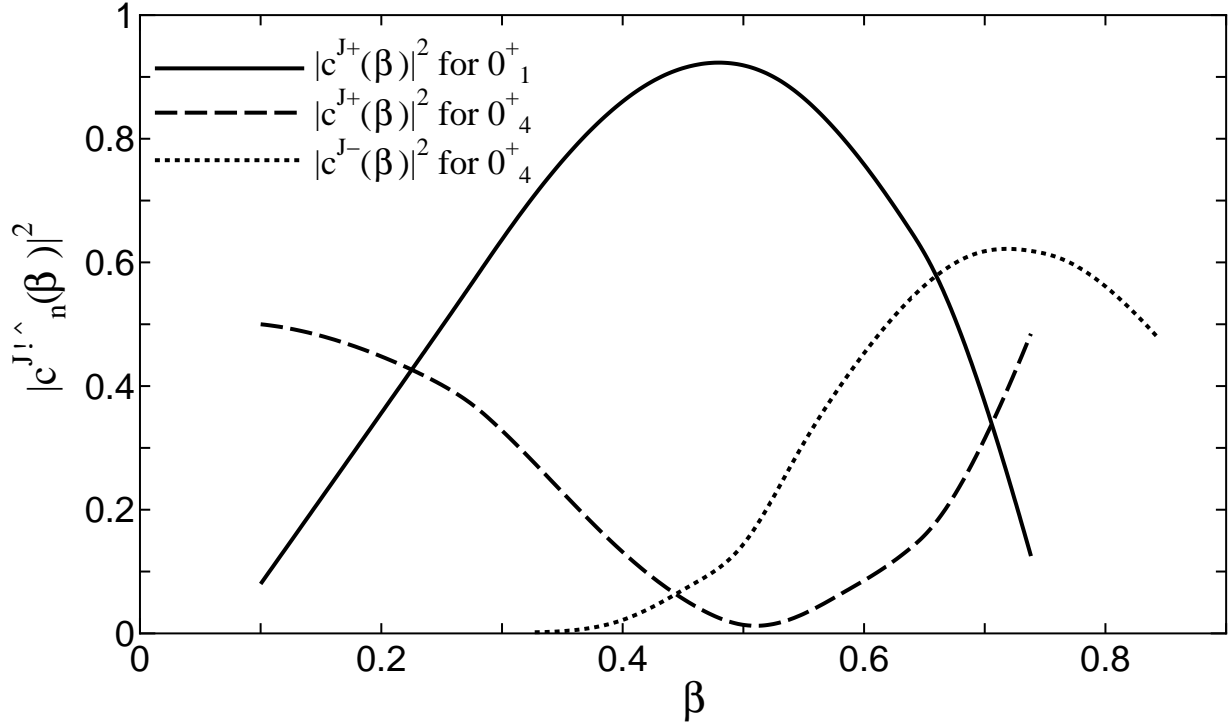


FIG. 8: The GCM amplitudes for 0_1^+ (solid line) and 0_4^+ (dashed line and dotted line) states. The definition of the GCM amplitude is given in the text.

MeV and 8.3 MeV, respectively.

We consider it worthwhile to discuss how the prominent $\alpha+^{16}\text{O}$ cluster structure of this band compared to the ground band is derived in the present calculation. As explained in section II, we include all of the obtained intrinsic wave functions as the GCM basis. The prominent $\alpha+^{16}\text{O}$ cluster structure is due to the considerable contribution of the $\Phi_{int(-)}(\beta)$ which was obtained by the variational calculation after the projection to negative-parity. When we include only $P_{MK=0}^{J^+}\Phi_{int(+)}(\beta)$ in the GCM basis, the content of $\alpha+^{16}\text{O}$ components of $K^\pi=0_4^+$ band members is around 40~70% (bracketed numbers in the third column of Table II) and comparable with that of the ground band. In contrast, when we include the $P_{MK=0}^{J^+}\Phi_{int(-)}(\beta)$ as well as $P_{MK=0}^{J^+}\Phi_{int(+)}(\beta)$, the $\alpha+^{16}\text{O}$ cluster structure of this band becomes prominent (numbers in the third column of Table II). In the outside of nucleus, the contribution from $P_{MK=0}^{J^+}\Phi_{int(-)}(\beta)$ (dotted line in Fig. 8) becomes larger, while in the inside $P_{MK=0}^{J^+}\Phi_{int(+)}(\beta)$ (dashed line in Fig. 8) is dominant. Therefore, in the outside of nucleus, the $\alpha+^{16}\text{O}$ cluster structure is prominent, which leads to a large α decay width. However, in the inside, the mean-field-like structure contributes to some extent and it leads to the

TABLE V: Observed and calculated intra-band $E2$ transition probabilities $B(E2; J_i^\pi \rightarrow J_f^\pi)$ [$e^2 \text{fm}^4$] within the $K^\pi=2^-$ band. For comparison, the results of the $j-j$ shell model (SM) [21] and $(\alpha+^{16}\text{O})+(^8\text{Be}+^{12}\text{C})$ coupled channel OCM (OCM) [20] are also shown. The effective charges which were used in each calculation are given in the bottom line.

$J_i^\pi \rightarrow J_f^\pi$	EXP	SM	OCM	AMD+GCM
$3_1^- \rightarrow 2^-$	113 ± 29	97	108	102.8
$4^- \rightarrow 3_1^-$	77 ± 16	75	77	77.8
$4^- \rightarrow 2^-$	34 ± 6	36	34	38.5
$5_1^- \rightarrow 4^-$	< 808	44	45	84.5
$5_1^- \rightarrow 3_1^-$	84 ± 19	48	49	56.6
$6^- \rightarrow 5_1^-$	32 ± 13	32	34	29.9
$6^- \rightarrow 4^-$	55^{+23}_{-13}	51	67	64.0
$\delta e/e$		0.8	0.069	0

existence of the small non- $\alpha+^{16}\text{O}$ component. It is interesting that though $P_{MK=0}^+ \Phi_{int(-)}(\beta)$ is less bound than $P_{MK=0}^+ \Phi_{int(+)}(\beta)$, $P_{MK=0}^+ \Phi_{int(-)}(\beta)$ contributes to this band.

4. $K^\pi = 2^-$ band

The $K^\pi=2^-$ band is the lowest negative-parity band. It starts from the 2^- state at 4.97 MeV and is observed up to the 9^- state, and exhibits a good rotational spectrum. The obtained excitation energy of the 2^- state is 6.51 MeV and we have calculated up to the 6^- state.

This band has a quite different character from the other three bands. From the shell model calculations, it is known that this band has a $(1p)^{-1}(sd)^5$ structure with respect to the ^{16}O core and the $SU_3(8,2)$ configuration is dominant, which means the absence of the $\alpha+^{16}\text{O}$ cluster structure and a large contribution from the spin-orbit force. Indeed, in the present result, the GCM wave functions of this band members consist of the wave functions on the $K^\pi=2^-$ curve and in the natural parity states ($\pi = (-)^J$), the mixing with the wave functions on the $K^\pi=0^-$ curve is quite small. As discussed in the previous subsection, the wave functions on the $K^\pi=2^-$ curve have a deformed mean-field-like character. Therefore,

the spherical-basis AMD gives much higher excitation energy of the 2^- state, 11.3 MeV. Though the character of the band is quite different from that of the $K^\pi=0_1^\pm$ band, the $B(E2)$ transition probabilities are again described well without any effective charges.

V. SUMMARY

In this study, we have presented the details of the new theoretical framework of deformed-basis AMD. This framework enables us to describe the coexistence, competition and mixing of the deformed mean-field structure and the cluster structure and gives us the proper evaluation of the spin-orbit force.

We have applied this framework to the ^{20}Ne nucleus. On the analysis of the obtained energy curves, three different characteristics of the nuclear structure appeared. The $J^\pi=1^-$ ($K^\pi=0^-$) curve has an almost pure $\alpha+^{16}\text{O}$ cluster structure, in which the spherical single-particle wave packets are localized into two parts. In contrast, the $J^\pi=2^-$ ($K^\pi=2^-$) curve has a deformed mean-field-like character in which the significantly deformed single particle wave packets are gathered around the center of the nucleus. The $J^\pi=0^+$ ($K^\pi=0^+$) curve has a mixed character. As the nuclear deformation becomes larger, the wave function gradually changes its structure from a deformed mean-field-like structure to a cluster structure.

By superposing the obtained wave functions, four rotational bands are obtained in the low-energy region. The $K^\pi=0_1^-$ band has an almost pure $\alpha+^{16}\text{O}$ cluster structure. Observed large α decay widths of this band members are reproduced and the obtained α -RWAs show a quite similar trend to those obtained by other cluster models. These facts mean that the cluster structure can exist as an independent degree of freedom of the nuclear excitation, even though the deformation of the mean-field and the effects of the spin-orbit force are included in the model space. The ground band has a mixed character of the deformed mean-field structure and the cluster structure. Because of the mixture of the deformed mean-field character, the obtained intra-band $E2$ transition probabilities are enlarged compared to the cluster models and the observed values are reproduced without any effective charge. The structure change along the yrast line is also investigated. As the angular momentum becomes larger, the deformed mean-field component in the wave function increases and the spin-orbit force acts strongly. By including the wave functions which have an almost pure $\alpha+^{16}\text{O}$ structure as the GCM basis, the $K^\pi=0_4^+$ band acquires a prominent cluster structure and

observed large α decay widths are reproduced. The $K^\pi=2^-$ band has a different character from the other three bands. The wave functions of this band member have a deformed mean-field character. The intra-band $E2$ transition probabilities are again reproduced without any effective charge.

Though these four bands have different characteristics, deformed-basis AMD successfully describes the coexistence and mixture of the cluster structure and mean-field structure in the same nucleus. Therefore, we believe that deformed-basis AMD is one of the most powerful approaches to describe the interplay of the mean-field structure and the cluster structure and to study the cluster structure and exotic cluster-like structure in medium-heavy and neutron-rich nuclei.

Acknowledgments

The author would like to thank Professor H. Horiuchi for his encouragement and for many valuable discussions. He also thanks Dr. A. Dóte, Dr. Y. Kanada-En'yo and Dr. Y. Fujiwara for valuable discussions. Many of the computations were carried out by SX-5 at the Research Center for Nuclear Physics, Osaka University (RCNP). This work was partially performed under the Research Project for Study of Unstable Nuclei from Nuclear Cluster Aspect sponsored by the Institute of Physical and Chemical Research (RIKEN).

[1] Reviews: K. Ikeda, T. Marumori, R. Tamagaki, H. Tanaka, J. Hiura, H. Horiuchi, Y. Suzuki, F. Nemoto, H. Bandō, Y. Abe, N. Takigawa, M. Kamimura, K. Takada, Y. Akaishi and S. Nagata, *Prog. Theor. Phys. Suppl.* **52** (1972).
 K. Ikeda, R. Tamagaki, S. Saito, H. Horiuchi, A. Tohsaki-Suzuki and M. Kamimura, *Prog. Theor. Phys. Suppl.* **62** (1977).
 K. Ikeda, H. Horiuchi, S. Saito, Y. Fujiwara, M. Kamimura, K. Katō, Y. Suzuki, E. Uegaki, H. Furutani, H. Kanada, T. Kaneko, S. Nagata, H. Nishioka, S. Okabe, T. Sakuda, M. Seya, Y. Abe, Y. Kondō, T. Matsuse and A. Tohsaki-Suzuki, *Prog. Theor. Phys. Suppl.* **68** (1980).

[2] H. Friedrich and K. Langanke, *Nucl. Phys.* **A242**, 47 (1975)

[3] A recent review; F. Michel, S. Ohkubo and G. Reidemeister, *Prog. Theor. Phys. Suppl.* **132**

Chap. II (1998)

T. Sakuda and S. Ohkubo, Prog. Theor. Phys. Suppl. **132** Chap. IV (1998)

[4] T. Yamaya, K. Katori, M. Fujiwara, S. Kato and S. Ohkubo Prog. Theor. Phys. Suppl. **132** Chap. III (1998)

[5] I. Tanihata, H. Hamagaki, O. Hashimoto, S. Nagamiya, Y. Shida, N. Yoshikawa, O. Yamakawa, K. Sugimoto, T. Kobayashi, D. E. Greiner, N. Takahashi, and Y. Nojiri, Phys. Lett. **160B**, 380 (1985).

W. Mittig, J. M. Chouvel, Zhan Wen Long, L. Bianchi, A. Cunsolo, B. Fernandez, A. Foti, J. Gastebois, A. Gillibert, C. Gregoire, Y. Schutz, and C. Stephan, Phys. Rev. Lett. **59**, 1889 (1987).

D. L. Olson, B. L. Berman, D. E. Greiner, H. H. Heckman, P. J. Lindstrom, and G. D. Westfall, Phys. Rev. C **24**, 1529 (1984). T.Motobayashi, Y.Ikeda, Y.Ando, K.Ieki, M.Inoue, N.Iwasa, T.Kikuchi, M.Kurokawa, S.Moriya, S.Ogawa, H.Murakami, S.Shimoura, Y.Yanagisawa, T.Nakamura, Y.Watanabe, M.Ishihara, T.Teranishi, H.Okuno and R.F.Casten Phys. Lett. **B346**, 9 (1995).

[6] N.Fukunishi, T.Otsuka and T.Sebe, Phys. Lett. **B296**, 279 (1992).
 Y.Utsuno, T.Otsuka, T.Mizusaki and M.Honma, Phys. Rev. **C64**, 011301 (2001).

A.Ozawa, T.Kobayashi, T.Suzuki, K.Yoshida and I.Tanihata, Phys. Rev. Lett. **84**, 5493 (2000).

[7] N.Itagaki, S.Okabe and K.Ikeda, Prog. Theor. Phys. Suppl. **142** 297 (2001).
 Y. Kanada-En'yo and H. Horiuchi Prog. Theor. Phys. Suppl. **142** 205 (2001).

[8] Y.Kanada-En'yo and H.Horiuchi, Phys. Rev. **C68**, 014319 (2003).

[9] M. Kimura and H. Horiuchi, Prog. Theor. Phys.(Kyoto) **107**, 33 (2002).

[10] K. P. Artemov, V. Z. Gol'dberg, I. P. Petrov, V. P. Rudakov, I. N. Serikov and V. A. Timofeev, Soviet J. Nucl. Phys. **24**, 1 (1976).

- [11] H. Horiuchi and K. Ikeda, *Prog. Theor. Phys.* **40** 277, (1968).
- [12] T. Tomoda and A. Arima, *Nucl. Phys.* **A303** 217, (1978).
- [13] A.Ono, H.Horiuchi, T.Maruyama and A.Ohnishi, *Prog. Theor. Phys.* **87**, 1185 (1992).
- [14] Y.Kanada-Enyo and H.Horiuchi, *Prog. Theor. Phys.* **93**, 115 (1995).
- [15] S.Takami, K.Yabana and K.Ikeda, *Prog. Theor. Phys.* 96, 407 (1996).
- [16] Y.Sugawa, M.Kimura and H.Horiuchi, *Prog. Theor. Phys.* **106**, 1129, 1153 (2001)
- [17] A.Dote, H.Horiuchi and Y.Kanada-Enyo, *Phys. Rev.* **C56** 1844, (1997).
- [18] K. Yazaki, *Prog. Theor. Phys.* **49** 1205, (1973).
- [19] T. Matsuse, M. Kamimura and Y. Fukushima, *Prog. Theor. Phys.* **53** 706, (1975).
- [20] Y. Fujiwara, H. Horiuchi and R. Tamagaki, *Prog. Theor. Phys.* **62** 122, (1979).
- [21] D. W. O. Rogers, K. W. Allen, H. C. Evans, N. A. Jelly, A. E. Litherland and B. Y. Underwood, *Phys. Letters* B37 65, (1971).
- [22] M. Dufour, P. Descouvemont and D.Baye, *Phys. Rev.* **C50** 795, (1994)

APPENDIX: REDUCED WIDTH AMPLITUDE OF THE AMD WAVE FUNCTION

The calculational methods for the α reduced width amplitude (α -RWA), α decay width and the square amplitude of the $\alpha+^{16}\text{O}$ component are briefly given. The method for evaluating these quantities from the AMD wave function was developed by Y. Kanada-En'yo [8] and the reader is directed to references [1, 8] for more details.

The $\alpha+^{16}\text{O}$ system is generally expressed by the RGM-type wave function.

$$\Phi_{\alpha+^{16}\text{O}}^{J\pi} = n_0 \mathcal{A}\{\chi_J(r)Y_{J0}(\hat{r})\phi(\alpha)\phi(^{16}\text{O})\}, \quad (\text{A.1})$$

$$n_0 = \sqrt{16! \cdot 4!/20!}, \quad \pi = (-)^J. \quad (\text{A.2})$$

Here, \mathcal{A} is the antisymmetrizer, \mathbf{r} is the relative coordinate between α and ^{16}O , $\phi(\alpha)$ and $\phi(^{16}\text{O})$ are the normalized internal wave functions of the clusters. $\chi_J(r)$ is the radial wave function of the relative motion between α and ^{16}O , and so normalized that $\Phi_{\alpha+^{16}\text{O}}^J$ is normalized to unity.

The normalized deformed-base AMD+GCM wave function $\Phi_M^{J\pi}$ of ^{20}Ne is divided into the $\alpha+^{16}\text{O}$ component and the residual part $\Phi_R^{J\pi}$.

$$\Phi_M^{J\pi} = \alpha\Phi_{\alpha+^{16}\text{O}}^{J\pi} + \sqrt{1-\alpha^2}\Phi_R^{J\pi}. \quad (\text{A.3})$$

$\Phi_R^{J\pi}$ is also normalized and orthogonal to the $\Phi_{\alpha+^{16}\text{O}}^{J\pi}$. We introduce the projection operator \mathcal{P}_L which projects out the $\alpha+^{16}\text{O}$ component from the $\Phi_M^{J\pi}$,

$$\begin{aligned} \mathcal{P}_L\Phi_M^{J\pi} &= \alpha\Phi_{\alpha+^{16}\text{O}}^{J\pi} \\ &= \alpha n_0 \mathcal{A}\{\chi_J(r)Y_{J0}(\hat{r})\phi(\alpha)\phi(^{16}\text{O})\}. \end{aligned} \quad (\text{A.4})$$

The practical formula for \mathcal{P}_L used in this study is given later. Using this projection operator, the squared amplitude of the $\alpha+^{16}\text{O}$ component W_J of $\Phi_M^{J\pi}$ is written as,

$$W_J \equiv |\alpha|^2 = \langle \Phi_M^{J\pi} | \mathcal{P}_L | \Phi_M^{J\pi} \rangle. \quad (\text{A.5})$$

The α -RWA $\mathcal{Y}_J(a)$ is defined as

$$\begin{aligned} \mathcal{Y}_J(a) &\equiv \frac{1}{n_0} \left\langle \frac{\delta(r-a)}{r^2} Y_{J0}(\hat{r}) \phi(\alpha) \phi(^{16}\text{O}) \right| \Phi_M^{J\pi} \rangle \\ &= \frac{\alpha}{n_0} \left(\frac{\delta(r-a)}{r^2} Y_{J0}(\hat{r}) \phi(\alpha) \phi(^{16}\text{O}) \right| \\ &\quad \times \left| \Phi_{\alpha+^{16}\text{O}}^{J\pi} \right\rangle, \end{aligned} \quad (\text{A.6})$$

and its squared amplitude $|a\mathcal{Y}(a)|^2$ is the probability to find α and ^{16}O clusters at the inter-cluster distance $r = a$. If we expand $\chi_J(r)$ with the radial wave function of the H.O. with the width parameter γ , $R_{NJ}(r, \gamma)$ as

$$\chi_J(r) = \sum_N e_{NJ} R_{NJ}(r, \gamma), \quad (\text{A.7})$$

the α -RWA is written as

$$\mathcal{Y}_J(a) = \alpha \sum_N \mu_N e_{NJ} R_{NJ}(a, \gamma). \quad (\text{A.8})$$

This means that when e_N is obtained, $\mathcal{Y}(a)$ is expanded by the H.O. wave function. Here, the eigenvalue of the RGM norm kernel μ_N is defined as

$$\begin{aligned} \mu_N = & \langle R_{nJ}(r) Y_{J0}(\hat{r}) \phi(\alpha) \phi(^{16}\text{O}) | \\ & \mathcal{A}\{R_{nJ}(r) Y_{J0}(\hat{r}) \phi(\alpha) \phi(^{16}\text{O})\} \rangle, \end{aligned} \quad (\text{A.9})$$

and its value is analytically evaluated. We calculate α decay width Γ_α using the α -RWA.

$$\begin{aligned} \Gamma_\alpha &= 2P_J(a)\gamma^2(a), \\ P_J(a) &= \frac{ka}{F_L^2(ka) + G_L^2(ka)}, \\ \gamma^2(a) &= \frac{\hbar^2}{2ma} |a\mathcal{Y}_L(a)|^2, \end{aligned} \quad (\text{A.10})$$

where F_L and G_L are the regular and irregular Coulomb functions, k is the wave number of the resonance energy, and a is the channel radius, which is chosen to be $a = 6\text{fm}$.

To evaluate W_J and $\mathcal{Y}_J(a)$, we have approximated the projection operator \mathcal{P}_L with the set of the orthonormalized angular-momentum-projected Brink wave functions. We start from the Brink wave function $\varphi_B(R_i)$ in which α and ^{16}O are represented by the SU_3 -limit wave functions which are located at the points $(0, 0, \frac{16}{20}R_i)$ and $(0, 0, -\frac{4}{20}R_i)$, respectively,

$$\varphi_B(R_i) = n_0 \mathcal{A}\{\varphi(\alpha, \frac{16}{20}\mathbf{R}_i), \varphi(^{16}\text{O}, -\frac{4}{20}\mathbf{R}_i)\}, \quad (\text{A.11})$$

$$\mathbf{R}_i \equiv (0, 0, R_i). \quad (\text{A.12})$$

The width parameters of α and ^{16}O are taken to be the same value ν for simplicity. By separating the center-of-mass wave function $\omega(\mathbf{X}_G)$, the internal wave function $\varphi_C(R_i)$ is written as

$$\varphi_B(R_i) = \omega(\mathbf{X}_G)\varphi_C(R_i), \quad (\text{A.13})$$

$$\varphi_C(R_i) = n_0 \mathcal{A}\{\Gamma(\mathbf{r}, \mathbf{R}_i, \gamma)\phi(\alpha) \phi(^{16}\text{O})\}, \quad (\text{A.14})$$

$$\Gamma(\mathbf{r}, \mathbf{R}_i, \gamma) = \left(\frac{2\gamma}{\pi}\right)^{3/4} e^{-\gamma(\mathbf{r}-\mathbf{R}_i)^2}, \quad (\text{A.15})$$

$$\omega(\mathbf{X}_G) = \left(\frac{20 \cdot 2\nu}{\pi}\right)^{3/4} \exp(-20\nu\mathbf{X}_G^2), \quad (\text{A.16})$$

$$\mathbf{X}_G = \frac{1}{20} \sum_{i=1}^{20} \mathbf{r}_i, \quad \gamma = \frac{16 \cdot 4}{20} \nu, \quad (\text{A.17})$$

where $\Gamma(\mathbf{r}, \mathbf{R}_i, \gamma)$ is the relative wave function between α and ^{16}O of the Brink wave function. The angular-momentum-projected Brink wave function $\phi_C^J(R_i)$ is obtained from the $\phi_C(R_i)$,

$$\varphi_C^J(R_i) = q_i^J P_{00}^J \varphi_C(R_i). \quad (\text{A.18})$$

P_{00}^J is the angular momentum projector and q_i^J is the normalization factor. The orthonormalized set of the angular-momentum-projected Brink wave functions $\tilde{\varphi}_\alpha^J$ is described by the linear combination of the $\varphi_C^J(R_i)$,

$$\tilde{\varphi}_\alpha^J = \frac{1}{\sqrt{\rho_\alpha}} \sum_i c_{i\alpha} \varphi_C^J(R_i), \quad (\text{A.19})$$

and the coefficients ρ_α and $c_{i\alpha}$ are the eigenvalues and eigenvectors of the overlap matrix $B_{ij} = \langle \varphi_C^J(R_i) | \varphi_C^J(R_j) \rangle$,

$$B_{ij} c_{i\alpha} = \rho_\alpha c_{i\alpha}. \quad (\text{A.20})$$

If enough numbers of the basis wave function $\tilde{\varphi}_\alpha^J$ are used, the projection operator \mathcal{P}_L is approximated by the set of $\tilde{\varphi}_\alpha^J$,

$$\begin{aligned} \mathcal{P}_L &\simeq \sum_\alpha |\tilde{\varphi}_\alpha^J\rangle \langle \tilde{\varphi}_\alpha^J|, \\ &= \sum_{ij} B_{ji}^{-1} |\varphi_C^J(R_i)\rangle \langle \varphi_C^J(R_j)|. \end{aligned} \quad (\text{A.21})$$

In the present calculation, we have employed 22 Brink-wave functions in which R_i is taken as $R_i = 0.5, 1.0, 1.5, \dots, 11.0$ fm.

Using Eq. (A.21), Eq. (A.4) and Eq. (A.5) are rewritten as

$$\begin{aligned} \mathcal{P}_L \Phi_M^{J\pi} &= \alpha n_0 \mathcal{A} \{ \chi_J(r) Y_{J0}(\hat{r}) \phi(\alpha) \phi(^{16}\text{O}) \}, \\ &\simeq \sum_{ij} B_{ji}^{-1} \langle \varphi_C^J(R_j) | \Phi_M^{J\pi} \rangle | \varphi_C^J(R_i) \rangle, \end{aligned} \quad (\text{A.22})$$

$$\begin{aligned} |\alpha|^2 &\simeq \sum_{ij} \langle \varphi_C^J(R_j) | \Phi_M^{J\pi} \rangle B_{ji}^{-1} \\ &\quad \times \langle \Phi_M^{J\pi} | \varphi_C^J(R_i) \rangle. \end{aligned} \quad (\text{A.23})$$

The expansion coefficient e_N of $\chi_J(r)$ and $\mathcal{Y}(a)$ is obtained from Eq. (A.22). We expand

the wave function of the relative motion $\gamma(\mathbf{r}, \mathbf{R}_i, \gamma)$ of Eq. (A.24),

$$\Gamma(\mathbf{r}, \mathbf{R}_i, \gamma) = e^{-\frac{\gamma}{2}R_i^2} \sum_{NJm} \left\{ \frac{(\gamma R_i^2)^{\frac{N}{2}}}{\sqrt{N!}} \times \sqrt{\frac{4\pi}{2J+1}} A_J^N Y_{Jm}(\hat{R}_i) R_{NJ}(r, \gamma) Y_{Jm}(\hat{r}) \right\}, \quad (\text{A.24})$$

$$A_J^N \equiv (-)^{(N-J)/2} \sqrt{\frac{(2J+1) \cdot N!}{(N-J)!! \cdot (N+J+1)!!}}. \quad (\text{A.25})$$

And using Eq. (A.14) and (A.24), Eq. (A.18) is rewritten as

$$\varphi_C^J(R_i) = n_0 \mathcal{A} \{ \chi_J^{(i)}(r) Y_{J0}(\hat{r}) \phi(\alpha) \phi(^{16}\text{O}) \}, \quad (\text{A.26})$$

$$\chi_J^{(i)}(r) = q_i^J e^{-\frac{\gamma}{2}R_i^2} \sum_N \frac{(\gamma R_i^2)^{\frac{N}{2}}}{\sqrt{N!}} A_J^N R_{NJ}(r). \quad (\text{A.27})$$

By inserting Eq. (A.26) into Eq. (A.22), we obtain $\chi_J(r)$ as a superposition of $\chi_J^{(i)}(r)$,

$$\chi_J(r) \simeq \frac{1}{\alpha} \sum_{ij} \langle \varphi_C^J(R_j) | \Phi_M^{J\pi} \rangle B_{ji}^{-1} \chi_J^{(i)}(r). \quad (\text{A.28})$$

Inserting Eq. (A.8) and (A.27) into Eq. (A.28), e_N is given as

$$e_N = \frac{1}{\alpha} A_J^N \sum_{ij} \left\{ \langle \varphi_C^J(R_j) | \Phi_M^{J\pi} \rangle B_{ji}^{-1} \times q_i^J e^{-\frac{\gamma}{2}R_i^2} \frac{(\gamma R_i^2)^{\frac{N}{2}}}{\sqrt{N!}} \right\}. \quad (\text{A.29})$$